

## Visible Emission Line Coronagraph (VELC) onboard ADITYA-L1

Jagdev Singh<sup>1</sup> · R. Ramesh<sup>1</sup> · B.  
Raghavendra Prasad<sup>1</sup> · V. Muthu Priyal<sup>1</sup> ·  
K. Sasikumar Raja<sup>1</sup> · S.N. Venkata<sup>1</sup> · P.U.  
Kamath<sup>1</sup> · V. Natarajan<sup>1</sup> · S.  
Pawankumar<sup>1</sup> · V.U. Sanal Krishnan<sup>1</sup> · P.  
Savarimuthu<sup>1</sup> · Shalabh Mishra<sup>1</sup> ·  
Varun Kumar<sup>1</sup> · Chavali Sumana<sup>1</sup> · S.  
Bhavana Hegde<sup>1</sup> · D. Utkarsha<sup>1</sup> ·  
Amit Kumar<sup>1</sup> · S. Nagabhushana<sup>1</sup> · S.  
Kathiravan<sup>1</sup> · P. Vemareddy<sup>1</sup> · C.  
Kathiravan<sup>1</sup> · K. Nagaraju<sup>1</sup> · Belur  
Ravindra<sup>1</sup> · Wageesh Mishra<sup>1</sup>

© The author(s) ●●●●

**Abstract** ADITYA L1, India's first dedicated mission to study Sun and its atmosphere from the Sun-Earth Lagrangian L1 location was successfully launched on September 2, 2023 with seven payloads. Visible Emission Line Coronagraph (VELC) is a major payload on ADITYA-L1. VELC has provision to carry out imaging and spectroscopic observations (the latter in three emission lines of the corona), simultaneously. Images of the solar corona in continuum at 5000Å, with the field of view (FoV) from  $1.05R_{\odot}$  to  $3R_{\odot}$  can be obtained at variable intervals depending on the data volume that can be downloaded. Spectroscopic observations of solar corona in three emission lines, namely 5303Å [Fe XIV], 7892Å [Fe XI], and 10747Å [Fe XIII] are possible simultaneously, with different exposure times and cadence. Four slits, each of width  $50\mu\text{m}$ , separated by 3.75mm helps to simultaneously obtain spectra at four positions in the solar corona at all the aforementioned lines. A Linear Scan Mechanism (LSM) makes it possible to scan the solar corona up to  $\pm 1.5R_{\odot}$  with variable step size. The instrument has the facility to carry out spectropolarimetric observations at 10747Å also in the FoV range  $1.05\text{-}1.5R_{\odot}$ . Various components of the instrument were tested interferometrically on the optical bench before installation. The individual components

---

✉ R.Ramesh  
[ramesh@iiap.res.in](mailto:ramesh@iiap.res.in)

<sup>1</sup> Indian Institute of Astrophysics, Koramangala, Bengaluru - 560034

were aligned and performance of the payload was checked in the laboratory using laser source and tungsten lamp. Wavelength calibration of the instrument was verified using Sun as a light source. All the detectors were calibrated for different parameters such as dark current and its variation with exposure time. Here, we discuss the various features of the VELC, alignment, calibration, performance, possible observations, initial data analysis and results of initial tests conducted in-orbit.

**Keywords:** Sun: corona, Sun: oscillations, Sun: magnetic fields

## 1. Introduction

The atmosphere of the Sun is highly dynamic, where the variations occur with periods ranging from seconds to years. Further, physical nature of solar coronal structures are very complex. The energetic events occurring at the Sun leads to solar flares and coronal mass ejections those affect the space weather and cause disturbances on the Earth. Sometimes during very energetic events and coronal mass ejections (CMEs), electrical grids and communication systems get damaged. To minimize the effect of such happenings, the Sun and its atmosphere need to be monitored all the time, 24 hours a day throughout the year. Apart from this, the plasma in the solar corona gets heated up to millions of degrees as compared to surface temperature of the Sun at  $5700^{\circ}\text{K}$ . There are various models to explain the heating of solar corona such as, wave heating of solar corona or impulsive heating of solar corona. The role of these processes need to be delineated. There are also contradictions in explaining the flows and/or waves in the solar corona. If there are waves and if these waves get damped, then, at what height these are damped?

The invention of coronagraph by Lyot in 1930 enabled observations of the extended coronal atmosphere of the Sun by blocking the solar disk. This invention opened the doors to study solar corona without the occurrence a total solar eclipse, with ground based coronagraphs as well as space based instruments. Various space missions such as SOLar and Heliopsheric Observastory (SOHO), Solar Dynamics Observatory (SDO), STEREO, Transition Region And Coronal Explorer (TRACE), Ulysses, Hinode, Solar Orbiter (SO), Parker Solar Probe (PSP) and many others have observed the Sun and its atmosphere in different wavelength domains such as X-rays, Ultraviolet (UV) and Extreme Ultraviolet (EUV). We have planned visible emission line coronagraph considering some of the following works done.

Most of the spectroscopic or imaging data in the visible wavelength range have been recorded during the total solar eclipses or using coronagraphs during excellent clear sky conditions (Pasachoff, et al. 2002; Raju, Chandrasekhar, and Ashok 2011; Voulgaris et al. 2012; Koutchmy, and Nitschelm 1983; Ichimoto et al. 1995; Singh, Bappu, and Saxena 1982; Singh, Sakurai, and Ichimoto 2003a; Singh et al. 2003b, 2004a,b; Singh, Sakurai, and Ichimoto 2006; Singh et al. 2011a; Samanta et al. 2016; Rusin, and Minarovjeh 1994; Minarovjeh et al. 2003). The observations during total solar eclipses provide data with minimum of

scattered light by the Earth's atmosphere. The advantage of coronagraphs in the visible wavelengths is that information with height from the solar limb becomes available and for relatively longer duration (Singh et al. 2004b). Spectroscopic observations in the transition region spectral lines obtained in the UV and EUV wavelength band provide information up to about  $1.2R_{\odot}$  (Hassler, Rottman, and Orrall 1990; Doyle, Banerjee, and Perez 1998). These correspond to plasma at relatively low temperatures compared to that of coronal plasma. In the X-ray wavelength domain, most of the observations have been made either by imaging the corona to study dynamics of coronal structures as function of height (Krishna Prasad, Singh, and Ichimoto 2013) or by performing spectroscopy of coronal loops on the solar disk to investigate their physical and dynamical properties as a function of distance from the base to the edge of the loop (Krishna Prasad et al. 2017). This way the true height from the solar limb is not known. Also, the signal gets integrated with the background solar disk and height along the loop. Spectroscopic observations of energetic events have been made in the emission lines in the X-ray wavelength range during the occurrence of jets which propagate outwards from the solar limb (Jelinek et al. 2015). The oscillations in the Doppler velocity with a period of  $\approx 300$ sec were detected by Tsubaki (1977) at some locations along the slit while observing in  $5303\text{\AA}$  emission line. Koutchmy, and Nitschelm (1983) found velocity oscillations with periods near 300sec, 80sec and 43sec from the time sequence spectra in the  $5303\text{\AA}$  line at  $1.04R_{\odot}$ . But they did not find any prominent intensity fluctuations during the period of observations. Singh et al. (1997) found intensity oscillations in the solar corona having periods of 56.5sec, 19.5sec, 13.5sec, 8.0sec, 6.1sec, and 5.3sec with amplitudes in the range of 0.2–1.3% of the coronal brightness.

Singh et al. (1999); Singh, Sakurai, and Ichimoto (2003a); Singh et al. (2003b, 2004b); Singh, Sakurai, and Ichimoto (2006) made systematic observations of the solar corona in four emission lines simultaneously during the period 1997–2007 with the 25cm coronagraph at Norikura observatory, Japan. Most of the time they could observe the solar corona between  $1.01R_{\odot}$  and  $1.20R_{\odot}$  in the  $5303\text{\AA}$ ,  $6374\text{\AA}$ ,  $7892\text{\AA}$ ,  $10,747\text{\AA}$  and  $10,798\text{\AA}$  coronal emission lines. They could carry out spectroscopic observations up to  $1.5R_{\odot}$  only on couple of days only because of limited number of hours of clear coronagraphic skies. Raju, Chandrasekhar, and Ashok (2011) found that width of the  $5303\text{\AA}$  emission line does not vary with height above the solar limb using data obtained with Fabry-Perot technique during the total solar eclipse of 2001 June 21 from Lusaka. But Singh et al. (1999); Singh, Sakurai, and Ichimoto (2003a); Singh et al. (2003b, 2004b); Singh, Sakurai, and Ichimoto (2006), and Krishna Prasad, Singh, and Ichimoto (2013) found variation in all the emission lines with height above the limb in the large number of observations made during the period 1997–2007 with 25cm coronagraph. The observations in different emission lines obtained on different days and of different coronal regions indicate similar behavior irrespective of shape, size and direction in the sky plane. They found decrease in the line width with height in the [Fe XIV] line and increase in line width with height in [Fe X] ( $6374\text{\AA}$ ) and [Fe XI] emission lines. The [Fe XIII] emission line width shows small increase or decrease with height. The magnitude of increase/decrease with height varied in different coronal structure up to about  $1.20R_{\odot}$  in all the observations.

The reason for not detecting the decrease in line width of the green line with height (Raju, Chandrasekhar, and Ashok 2011) may be due to low spectral resolution (26,000) in the Fabry-Perot interferometer as compared to 4,80,000 of the spectroscopic observations. Singh, Sakurai, and Ichimoto (2006) could obtain a raster scan of spectra in the [Fe X] and [Fe XIV] emission lines with long exposure time for each spectra from 1.01 to  $1.5R_{\odot}$  on October 26, 2003 due to availability of long hours of excellent clear skies. They found that line widths of [Fe X] increase whereas that of [Fe XIV] decreases with height above the limb. The increase and decrease of line width happens up to about  $200''$  above the limb but remains the same beyond this height.

Further, these observations indicate that intensity ratio of [Fe XI]/[Fe X] increases with height above the limb whereas that of [Fe XIV]/[Fe X] and [Fe XIV]/[Fe XIII] decreases with height above the limb (Singh et al. 2004b; Krishna Prasad, Singh, and Ichimoto 2013). The systematic observations show that variations in the intensity ratios and line widths for different lines are complex. Similarly, the line width ratio [Fe X]/[Fe XI] increases whereas that [Fe XIV]/[Fe X] decreases with height above the limb. These results imply that loop tops are hotter as compared to the foot points if observed in [Fe X] and [Fe XI] emission lines, and loop tops are cooler if observed in [Fe XIV] and [Fe XIII] emission lines. This type of phenomena is difficult to visualize and explain. Such type of variation in the parameters of emission lines is contradictory, considering the abundances of these ions as function of temperature. It may be noted that these results are based on the observations up to about  $1.2R_{\odot}$  only. It is still not known how the intensity ratios vary beyond  $1.2R_{\odot}$ . Such type of behavior of the coronal emission lines needs to be confirmed and investigated further by carrying out systematic observations. It may also be noted that spectral resolution of observations made in the visible part of the spectrum is much larger than that in UV, EUV and X-rays.

In view of the projected science objectives to study the physical and dynamical structure of solar corona, space weather by monitoring the occurrence and dynamics of CMEs, magnetic topology of solar corona and address the heating mechanism of coronal plasma, VELC was developed (Singh et al. 2011b). We have planned the imaging of solar corona at  $5000\text{\AA}$  over the FOV  $1.05\text{-}3R_{\odot}$ , and spectroscopy around three emission lines ( $7892\text{\AA}$ ,  $10747\text{\AA}$ , and  $5303\text{\AA}$ ) over the FoV  $1.05\text{-}1.5R_{\odot}$ , simultaneously. We have listed the wavelength values of emission lines based on the ground measurements as most of the readers are familiar with the wavelengths of these emission lines. The filters have been designed taking into account their use in space (vacuum conditions) and the convergence of beam passing through the filter. Here, we discuss the requirement of the instrument, design, calibration and present status of the payload.

## 2. Requirement and Purpose of VELC

Observations of the solar corona during total solar eclipses can be carried out for few minutes only from any location along the totality path of the eclipse. Ground based observations using a coronagraph require excellent sky conditions

which generally are limited to a couple of hours and that too in select locations for minimal number of days in a year. Coronal observations in the visible emission lines provide better spectral resolution as compared to those in EUV and X-ray wavelengths. The LASCO-C1 Coronagraph onboard SOHO had the facility to observe the corona in visible emission line using Fabry-Perot etalon, but with comparatively lesser spectral resolution. To monitor the solar coronal energetic events 24 hours a day throughout the year, the requirement of a space coronagraph operating at visible wavelengths with better spectral resolution was realized. The Indian scientific community after number of meetings decided to have a space coronagraph with the following science objectives:

- Diagnostics of the coronal features (Temperature, Velocity & Density).
- To understand the processes involved in heating of the corona and solar wind acceleration.
- To study the origin, development and dynamics of CMEs.
- To study the dynamics of the large scale coronal transients.
- Studies on drivers for space weather.
- Measurement of coronal magnetic fields.

An internally occulted coronagraph was designed to carry out observations for the above mentioned scientific objectives. To study the physical and dynamical characteristics of coronal plasma and features such as coronal loops, spectroscopy in two or more emission lines is needed. Three emission lines were chosen to cover a temperature range of  $1-2 \times 10^6$  K. It is desirable to carry out observations as close to the solar limb as possible. Considering the pointing limitations of the satellite and scattering due to primary mirror it was decided to have observations in the heliocentric distance ( $r$ ) range  $1.05-3.0R_{\odot}$  for imaging, and  $1.05-1.5R_{\odot}$  for spectroscopy. Typically, observations with spatial resolution  $\approx 1-2''$ , spectral resolution  $\sim 10-100$  mÅ, and temporal resolution  $\sim 1-100$  sec are preferable to study the quiet corona and energetic events there. A two-beam arrangement was planned to perform spectro-polarimetric observations also. After preliminary optical design, feasibility studies were carried out with the vendors and various organisations of ISRO. The discussions indicated that the primary mirror of the coronagraph need to be 200mm instead of 300mm proposed initially. The size and weight of the payload imposed limitations. Three emission lines were chosen instead of four emission lines proposed. The focal length of the primary mirror and spectrograph lens were also reduced. The download limit of 100 Gigabit per day data restricted the provision to carry out high frequency (1 Hz) observations. Various parameters of the final design are listed in Table 1. Photon computations and other details are described in Kumar et al. (2018); Singh et al. (2019).

### **3. Optical design of VELC**

Considering the scientific aims mentioned in Section 2, the instrument should have facility to image the solar corona in continuum, perform spectroscopy in coronal emission lines, and spectropolarimetry to measure the polarization of solar corona. We planned to have these in a single payload by imaging the solar

**Table 1.** Parameters of the internally occulted mirror coronagraph

Parameter	Specification
Imaging of solar corona	At 5000Å with FoV up to $3R_{\odot}$
Spectroscopy of solar corona	FoV up to $1.5R_{\odot}$
Emission lines for spectroscopy	5303Å [Fe XIV], 7892Å [Fe XI], 10747Å [Fe XIII]
Primary mirror	Parabolic 195mm diameter, focal length = 1300mm, f-ratio = 6.67
Entrance Aperture	147mm
Littrow lens focal length	780mm
Multi-slit	4 slits, each of width $50\mu\text{m}$ ( $9.6''$ ), spacing between the slits = 3.75mm
Grating	600 lines/mm blazed at $42^{\circ}$
Pixel size of visible detector (sCMOS)	$6.5\mu\text{m}^2$
Pixel size of IR detector (InGaAs)	$25\mu\text{m}^2$
Plate scale	$2.25''/\text{pixel}$ (Continuum) $1.25''/\text{pixel}$ (5303Å & 7892Å) $4.33''/\text{pixel}$ (10747Å)
Spatial resolution	$4.5''$ (continuum) $2.5''$ (5303Å & 7892Å) $8.6''$ (10747Å)
Spectral Dispersion	$28.4\text{m}\text{Å}/\text{pixel}$ (Fe XIV, 4th order) $31.3\text{m}\text{Å}/\text{pixel}$ (Fe XI, 3rd order) $223.0\text{m}\text{Å}/\text{pixel}$ (Fe XIII, 2nd order)
Efficiency	$\approx 28\%$ (continuum channel) $\approx 5\%$ (spectral channels)

corona at 500nm, and carry out spectroscopy in emission lines at wavelength  $>500\text{nm}$  by splitting the coronal beam using a dichroic beam splitter. Based on the experience of observations with the 25cm coronagraph at Norikura observatory in Japan, we chose the emission lines for VELC. It has the facility to observe in three emission lines 5303Å, 7892Å, and 10747Å, simultaneously. The facility to observe in the 6374Å emission line could not be included because of increase in width and weight of the instrument. Simultaneous measurements of the line profiles in different emission lines are needed to derive the thermal and dynamic characteristics of coronal loops and structures. So we have used four detectors, one for the imaging in continuum and three for the above mentioned emission lines.

Data from observations close to the solar limb are very important to study the dynamics of CMEs and other coronal transients (see e.g. Ramesh, Subramanian, and Sastry 1999; Kathiravan, Ramesh, and Subramanian 2002; Ramesh, Kathiravan, and Sastry 2003; Kishore et al. 2015; Kumari et al. 2019). Most of the coronal structures in emission do not extend to large distances in the solar corona and therefore require observations close to the solar limb to investigate their physical and dynamical characteristics (Ramesh, Nataraj, and Kathiravan 2006). In view of the pointing accuracy and drift of the spacecraft in space, it

was decided to have field-of-view (FoV) from  $1.05R_{\odot}$ . The available detector size, and the need for high resolution in the spectral observations restricted the outer FoV to  $1.5R_{\odot}$  and  $3.0R_{\odot}$  for the spectroscopic and continuum observations, respectively. Due to the above mentioned inner limit of the FoV at  $1.05R_{\odot}$ , it was decided to develop an internally occulted coronagraph. In view of the spacecraft platform size, limit on the payload weight, VELC instrument was designed with the details mentioned in the following paragraphs.

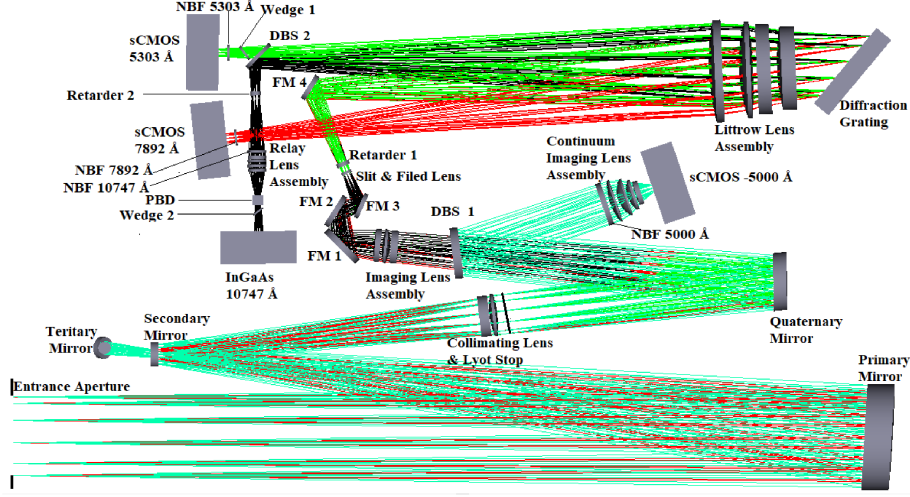


**Figure 1.** Optical Layout of the Visible Emission Line Coronagraph (VELC) onboard Aditya-L1.

Figure 1 shows the optical layout of VELC on board Aditya-L1 mission. The details of optical design and its performance are given in Kumar et al. (2018); Prasad et al. (2017); Singh et al. (2019). Off-axis concave parabolic mirror (M1) of VELC with focal length 1300mm has a clear aperture of 192mm. The mirror was cut from the parent parabola at an off-axis distance 152mm. M1 is mounted on the optical bench at a distance of 1570mm from Entrance Aperture (EA) of size 147mm to cover the desired FoV of  $3R_{\odot}$ . The diameter of solar disk beam will be 162mm on the primary mirror. For the coronal beam corresponding to the  $3R_{\odot}$  FoV, it will be 192mm. Secondary Mirror (M2), concave spherical with central elliptical hole is positioned at the focal plane of M1. Tertiary mirror (M3) installed behind M2 at an angle of  $45^{\circ}$  reflects the light up to  $0.28^{\circ}$  ( $1.05R_{\odot}$ ) into deep space through a small opening on the top cover of the payload. The small opening is made such a way that outside light does not enter into the instrument. Optical surface of M2 reflects the solar coronal light over the FoV  $1.05-3R_{\odot}$  towards the Collimator Lens Assembly (CLA), a two-lens system designed to re-image the EA in combination with M1 & M2, on the Lyot-stop. It is kept at the pupil plane of CLA, and stops the diffracted light from the EA proceeding to the quaternary mirror (M4) mirror. CLA collimates the coronal light over the FoV ( $1.05-3R_{\odot}$ ) and directs towards M4. The latter is an off-axis concave parabolic mirror with focal length 1180mm, off-axis distance 250 mm and clear

aperture 106mm. It directs the coronal light towards Dichroic Beam Splitter-1 (DBS-1) which reflects the coronal light  $< 5150\text{\AA}$  towards continuum channel for imaging the corona and transmits the coronal light  $> 5150\text{\AA}$  for spectroscopy observations. A four-element Imaging Lens Assembly-1 (ILA-1) forms the image of the solar corona with the light reflected from DBS-1. A narrow band filter with bandwidth of  $10\text{\AA}$  centred at  $5000\text{\AA}$  placed in front the lens assembly restricts the bandwidth of the continuum image of solar corona. Continuum images data are recorded by using a sCMOS camera of  $2592 \times 2192$  format with pixel size  $6.5\mu\text{m}^2$ . Plate scale of continuum channel is  $2.25''$  per pixel. Transmitted coronal light with wavelength  $> 5150\text{\AA}$  is focused by Imaging Lens Assembly-2 (ILA-2). The latter is a three-element lens and it forms colour corrected image of the solar corona over spectral band  $5150 - 11000\text{\AA}$  on the multi-slit assembly (MSA) of the spectrograph. A linear scan mechanism, consisting of two fold mirrors (FM-1 & FM-2) located between ILA-2 and slit plane, is used to scan the FoV across the slits. Another fold mirror FM3 directs the beam towards the MSA of the spectrograph.

Fold Mirror-4 (FM-4) guides the beam towards a Littrow Lens Assembly (LLA) consisting of four elements which act as collimator and camera lens. A diffraction grating is used to disperse the incident beam. The size of the LLA has been designed such that diffracted beam for all the three wavelengths (i.e.  $5303\text{\AA}$ ,  $7892\text{\AA}$ , and  $10747\text{\AA}$ ) do not have any intensity vignetting. The Littrow lens directly focuses the spectra around  $7892\text{\AA}$  (3rd order) emission line on the sCMOS detector. A narrow band filter (NBF) centred at  $7892\text{\AA}$  with  $8\text{\AA}$  pass band kept in front of the detector avoids the overlap of spectra due to the use of multiple (four) slits. Second order line at  $10747\text{\AA}$  and 4th order line at  $5303\text{\AA}$  lie almost in same direction. So, a Dichroic Beam Splitter-2 (DBS-2) with a small wedge to correct the vignetting for  $5303\text{\AA}$  spectra, is used to separate the two dispersed beams spectrally and spatially. DBS-2 transmits the spectral band around  $5303\text{\AA}$  and reflects the band around  $10747\text{\AA}$ . The transmitted spectra around  $5303\text{\AA}$  gets focused through a  $6\text{\AA}$  narrow band filter (NBF) which avoids the overlap of spectra due to the use of multiple slits. A polarization modulator (retarder) with rotation facility is present at the focal plane of  $10747\text{\AA}$  spectra, to add a defined amount of phase shift in terms of polarization to the light beam based on the rotation angle. The details about the polarization measurements are described in Nagaraju et al. (2021); Venkata, Prasad, and Singh (2021); Sasikumar et al. (2022); Venkata et al. (2024).

Because of space constraints to accommodate the detector at the focal plane of  $10747\text{\AA}$ , a Relay Lens Assembly (RLA) along with a NBF is used to re-image the spectra on the detector at a convenient location. A Polarizing Beam Displacer (PBD) assembly along with a wedge is mounted after the RLA to split the E- & O-rays to perform the polarization measurements. This arrangement permits the spectroscopic as well as polarization observations in the  $10747\text{\AA}$  emission line. The retarder remains stationary during spectroscopy and rotates during polarization observation. The retarder completes one rotation in 10.08 seconds. More details about the PBD, RLA and retarder are described in Sasikumar et al. (2022).



The payload was assembled, aligned, and tested for its performance in class 10 area of the laboratory to minimize molecular and particle deposition on the optical components of the instrument. Only two persons worked inside the laboratory at any given time to maintain its class 10 quality. In the following sections, we give details of some components of the payload.

### **3.1. Shutter with the neutral density (ND) filter**

A multi-time opening shutter has been mounted in front of the EA of the coronagraph. This shutter will be closed during the operation of spacecraft thrusters to avoid the contaminants from entering the instrument. The shutter has a neutral density (ND) filter of 50mm diameter and density 4, calibrated at the required wavelengths. The ND filter is of reflector type to minimize its heating due to sunlight. The transmission of the filter is  $0.56 \times 10^{-4}$ ,  $0.64 \times 10^{-4}$ ,  $1.51 \times 10^{-4}$ , and  $2.95 \times 10^{-4}$  at 5000Å, 5303Å, 7892Å, and 10747Å, respectively. The clear aperture of the ND filter is 45mm. The density of the ND filter, and ratio of the sizes of the EA and ND filter limits the intensity of the solar disk light in the shutter closed position to nearly same as that of the coronal light in shutter open condition. The purpose of the ND filter is to obtain images and spectra of solar disk by off-pointing the spacecraft in the shutter closed condition. This data will be used to convert the observed detector counts from the corona (during shutter open observations) in units of solar flux, i.e.  $\text{ergs}/\text{cm}^2/\text{sec}/\text{Å}/\text{sr}$ .

### **3.2. Primary Mirror M1**

The M1 mirror parent parabola was fabricated and super polished at the Laboratory for Electro-Optics Systems (LEOS), an ISRO organisation. Four mirrors were cut with an off-axis distance of 152mm. One of the off-axis mirrors with better quality was used in the flight model of the payload. To estimate the scatter from the mirror, measurements of micro-roughness were carried out with various plate scales in the range of  $20\mu\text{m}$  to 2.15mm with a profilometer in the laboratory. The measured micro-roughness is  $\approx 5\text{Å}$  for the plate scale of 2.15mm. The details about the micro-roughness and scatter measurements are given in Venkata et al. (2017).

### **3.3. M2 mirror as an occulter and reflector of coronal light**

Stainless steel was selected for the fabrication of M2 mirror to obtain sharp edge of the central hole, and coated with nickel using electrolysis process. The major and minor axes of the central hole of M2 are 13.05mm and 12.95mm, respectively. Clear aperture of the secondary mirror M2 is 40mm. The focal length is 700mm. The elliptical hole at the centre of M2 mirror acts as an internal occulter. Thus, the M2 mirror allows the solar disk and part of coronal light up to  $1.05R_{\odot}$  pass through it, and reflect the coronal light from 1.05 to  $3.0R_{\odot}$  for imaging and spectroscopic observations.

### 3.4. Multi-slit assembly

Multi-slit assembly (MSA) consisting of four slits was used to decrease the observing time by a factor of four for the spectroscopic observations over the required FoV. The MSA has four slits with separation of 3.75mm between each slit. Initially the width of the slits was proposed to be  $20\mu\text{m}$  to achieve high spatial resolution of  $3.8''$ . But the width of the slits was increased to  $50\mu\text{m}$  considering the availability of photons in the emission lines in the outer corona around  $1.3R_{\odot}$ , the drift of the spacecraft  $0.2''$  per second, and the exposure time required to get sufficient signal-to-noise ratio (SNR) for emission line profiles (Singh et al. 2019). The slit width has an accuracy of  $\pm 1\mu\text{m}$ . The separation and parallelism between the slits are accurate within  $\pm 5\mu\text{m}$ . The increase in slit width decreases the spatial resolution to  $9.2''$ , but sufficient for the emission line corona. Moreover, keeping  $20\mu\text{m}$  slit width would not have helped in view of the drift rate, pointing accuracy and the large exposure time required for the spectroscopic observations. The separation of 3.75mm between the slits has been optimized considering the dispersion of the spectra and the Full Width Half-Maximum (FWHM) of the narrow band filters.

### 3.5. Linear scan mechanism (LSM)

To obtain images of solar corona in the three emission lines mentioned above, we need to scan the image across the four slits. The separation between the slits is 3.75mm. The image can be scanned across each slit by  $\pm 1.875\text{mm}$ . The image shifts by  $20\mu\text{m}$  at the slit plane when LSM moves by  $10\mu\text{m}$ . Therefore, we need  $\pm 0.9375\text{mm}$  movement of LSM. For this purpose a Linear Scan Mechanism (LSM) was designed and developed at U R Rao Satellite Centre (URSC), an ISRO organisation. The requirement was movement insteps of  $10\mu\text{m}$  step size and, traverse of  $0.9375\text{mm}$  on either side of the middle position of LSM termed as 'home'. Movement of the LSM is read by an optical encoder. Two encoders are implemented (main and redundant). The LSM is designed for a travel range of  $\pm 1.2\text{mm}$  (i.e.  $\pm 1200\mu\text{m}$ ). Considering possible inadvertant over travel beyond  $\pm 0.9375\text{mm}$ , the LSM has a hardware stop switch at  $\pm 1.2\text{mm}$ . Before this limit, there is a software stop at  $\pm 1\text{mm}$ . The location of the four slits on the coronal image at 'home' position of LSM is shown in Figure 2. Two fold/flat mirrors FM1 and FM2 mounted on a single platform are at  $90^\circ$  to each other, with FM1 perpendicular to the incoming beam. This platform is mounted on the LSM which can be moved in a direction joining the centre of these two mirrors. The movement of LSM was tested in steps of  $10\mu\text{m}$  and its multiples by measuring the movement of the image of a laser beam on a detector. The pixel size in the latter is  $1.85\mu\text{m}$ , for accurate measurements. The measurements show a deviation of  $\pm 1\mu\text{m}$  for a step size of  $10\mu\text{m}$ .

### 3.6. Dispersion Grating

We planned to carry out spectroscopic observations simultaneously around 2nd order  $10747\text{\AA}$ , 3rd order  $7892\text{\AA}$  and 4th order  $5303\text{\AA}$  emission lines, with maximum possible efficiency at all the wavelengths. A grating with 600 grooves/mm,

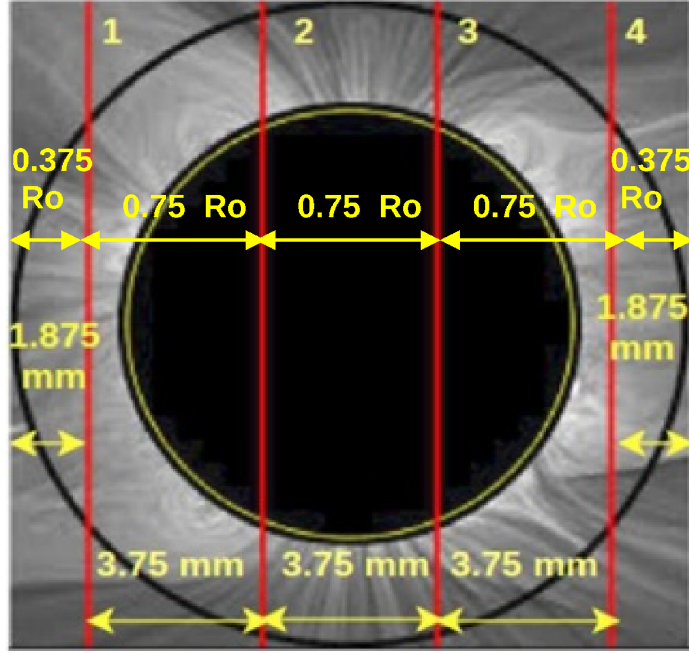


**Figure 2.** Location of the four slits in the VELC spectroscopy channel. The vertical red lines represent the four slits and their locations on a coronal image (obtained during a total solar eclipse) when the LSM is in its ‘home’ position. The separation between the slits is indicated by the horizontal yellow lines. The yellow circle at the center of the image represents the Sun disk size. The ‘filled’ black circular area indicates the extent of the ‘hole’ in the M2 mirror. The outer black circle indicates the FoV of VELC for spectrographic observations.

blazed at  $42^\circ$ , and of  $140\text{mm} \times 180\text{mm}$  size was required. We procured five replica gratings of the master grating fabricated with the specification mentioned above and used the first replica grating in the payload. With the optical set up of the instrument and this grating, the dispersion values are  $28\text{m}\text{\AA}$ ,  $31\text{m}\text{\AA}$  and  $223\text{m}\text{\AA}$  per pixel for  $5303\text{\AA}$ ,  $7892\text{\AA}$  and  $10747\text{\AA}$  emission lines, respectively.

### 3.7. Filters

As mentioned before, multi-slit assembly with four slits are used in VELC to decrease the observing time for generating images of the solar corona in the three emission lines. We had also planned to observe simultaneously in different wavelengths. Therefore we need to use narrowband filters to avoid overlap of spectra due to the different slits, and Dichroic beam splitters to separate the required wavelengths for each channel. We designed and then procured space qualified filters from Alluxa, Inc. The narrow band filters centred at  $5304.3\text{\AA}$ ,  $7893.9\text{\AA}$  and  $10749.3\text{\AA}$  (wavelengths in space) have bandwidths of  $6\text{\AA}$ ,  $8\text{\AA}$ , and  $11\text{\AA}$ , respectively. Their use in space and the shift in the passband of the filter in the converging beam were taken into consideration while specifying the central wavelength of the filters.

### 3.8. Detectors

We have used four detectors - three sCMOS based detectors for the visible wavelength observations and one InGaAs detector (henceforth called IR detector) for the 10747Å emission line. All the four detectors were designed, developed and tested by Space Applications Center, an ISRO organization. The performance of the chips was tested for the noise level at different operating temperatures. The noise decreases with operating temperature. In view of the noise and thermal design, it was decided to operate the sCMOS detectors at  $-5^{\circ}\text{C}$  and IR detector at  $-17^{\circ}\text{C}$ . The details of detector calibration and performance are given in Singh et al. (2022); Muthu Priyal et al. (2023). Some of the basic features of the detector are listed here: the sCMOS detectors have a  $2592 \times 2192$  format with a pixel size of  $6.5 \mu\text{m}^2$ . It has the facility of record the data in low and high gain, simultaneously. The low gains are 1X and 2X, high gains are 10X and 30X. Data can be obtained simultaneously in one low gain and one high gain. The full well capacity (FWC) is 30,000 electrons at 1X with 11-bit readout for both the gains. The IR camera has a  $640 \times 512$  format with a pixel size of  $25 \mu\text{m}^2$ . It can be operated in two modes, one low gain and other high gain, but only one at a time. The readout is 12-bit.

## 4. Alignment and integration of Payload

Based on the tolerance and performance analysis, fabrication specifications for each optical element and optical sub assemblies were generated. Individual optical elements were tested and their performance was evaluated prior to integrating them as the sub assemblies. Post realization of the sub-assemblies, they were subjected to the environmental tests and their performance was evaluated (Venkata et al. 2023a; 2023b). After completion of the testing and evaluation of the individual subsystems, they were aligned and integrated in the payload as per the pre-defined tolerances generated from the system level tolerance analysis. Alignment tolerances of optical sub-assemblies of VELC are listed in Table 2. The entire process of alignment and integration of VELC is divided into 4 major parts as mentioned below:

- Optical Bench Alignment
- Optical Axis Reference Establishment
- Alignment upto Spectrograph Slit Plane
- Alignment of Spectroscopic Channels

As mentioned in Table 2, primary mirror (M1), collimating lens and detectors are used as the compensators during the alignment process. The positions of these elements are adjusted in order to correct the aberrations / alignment errors of other optical elements, to meet performance requirements. In Section 4.1 we provide details of the alignment procedure for each stage.

**Table 2.** Alignment tolerances of optical sub-assemblies of VELC

Optical Sub-assembly	De-center Tolerance ( $\pm\mu\text{m}$ )	Tilt Tolerance ( $\pm\text{arcsec}$ )	Inter-separation Tolerance ( $\pm\mu\text{m}$ )
Primary Mirror (M1)	Compensator	Compensator	Compensator
Secondary Mirror (M2)	50	30	50
Tertiary Mirror (M3)	50	30	100
Quaternary Mirror (M4)	50	30	100
Collimating Lens	Compensator	Compensator	Compensator
Continuum Imaging Lens	50	30	100
Spectrograph Imaging Lens	50	30	100
Littrow Lens	50	30	250
Relay Lens	50	30	100
Diffraction grating	100	30	100
Dichroic Beam Splitters (DBS-1 & DBS-2)	100	30	100
Narrow Band Filters	100	30	100
Fold Mirrors (FM1, FM2, FM3, & FM4)	100	30	100
Detectors	Compensator	Compensator	Compensator

#### 4.1. Optical Bench Alignment

All the optical sub assemblies of VELC are supported on a light weight optical bench made of titanium, mounted on the satellite top deck. The surface area on the top side of the optical bench for mounting the sub-assemblies has a surface planarity/irregularity  $< \pm 20\mu\text{m}$ . The optical bench was mounted on a transfer trolley which is fixed to a vibration isolation table in ISO-4 class (Class-10) clean room. Prior to mounting the individual sub-assemblies, planarity of the optical bench was ensured. For this, the mounting interfaces at the four corners of the optical bench were considered. Mounting interfaces at the four corners of the optical bench are Entrance Aperture (EA), M1, Grating and 5303Å channel detector mounting (Figure 1). Optical bench planarity adjustment was carried out using a theodolite. The latter was fixed on a XYZ stage on top of a heavy duty tripod. A 100mm slip gauge was placed at the location of the EA mounting interface on the optical bench. Height and focus of the theodolite were adjusted such that the horizontal cross hair of the theodolite coincides with the top edge of the slip gauge. The reading of the theodolite was noted. The same experiment was repeated at the other three locations. In order to ensure the planarity of the optical bench, required shims (difference between values at EA, and other locations) were introduced in between the interfaces of the optical bench and the transfer trolley as per the values. The repeat of the experiment after fixing the shims indicated that the theodolite readings agree within  $4''$ .

#### 4.1.1. Optical Axis Reference Establishment

After establishing the planarity of the optical bench, the theodolite axis was aligned with the optical axis of the payload. Optical axis of VELC needs to be at a distance of 195mm (design value) from the corner of the optical bench at EA and M1 interfaces. Horizontal axis (H-axis) of the theodolite is adjusted to this with the help of slip gauges and theodolite. By design, the centers of all the optical components and the detector are at 130mm from the opto-mechanical interfaces at the top surface of optical bench. Therefore, the vertical axis of the theodolite, locations of EA and M1 were aligned to a height of 130 mm from the mounting interfaces on the top surface of the optical bench using 130mm slip gauge. Height of the theodolite was adjusted such that its cross hair coincides with the tip of the height gauge placed at EA and M1 with vertical axis reading at  $90^\circ$ . The tilt error between the horizontal axis of the theodolite and the optical axis is  $\approx 1.5''$  and  $\approx 2''$  between the vertical axis of the theodolite and the optical axis.

#### 4.1.2. Primary Mirror (M1) Alignment

M1 need to be aligned interferometrically in its nominal position to ensure that no aberrations are introduced. Two theodolites were used to align M1 mirror, theodolite-1 in front of EA, and theodolite-2 in the opposite direction half a meter away from M1 mirror. First, a reference flat was mounted at the M1 mounting interface and aligned with respect to theodolite-1 in auto-collimation mode. Then, a Zygo interferometer was aligned with respect to the optical axis of VELC using the reference flat. The position of the interferometer was fixed on the optical bench such that it is not disturbed during the entire process of aligning all the optical sub-assemblies on the optical bench. After aligning the interferometer, the actual flight mirror M1 was placed in its nominal position. Instead of the secondary mirror (M2), a flat mirror was mounted at the focal plane of M1. The flat mirror was adjusted such that the focused beam on it traces back the same path to the interferometer after reflection from M1 through EA. Wavefront error in the reflected beam from M1 was computed using the fringe pattern recorded by the interferometer. The RMS value was 8.34nm. After aligning M1 in its nominal position, the mounting screws were torqued to the optical bench while continuously monitoring the fringe pattern with the interferometer.

#### 4.1.3. Alignment of Secondary Mirror and Collimating Lens Assembly

For interferometric alignment of M2 and collimating lens, a custom-made spherical mirror with same radius of curvature as the secondary mirror of VELC with RMS surface figure  $\lambda/40$  was mounted at the secondary mirror location (M1 focus). Collimating Lens Assembly (CLA) was mounted in its nominal position in a free condition. With M2 (without central hole) and CLA in position, wavefront error of the transmitted beam after the CLA was measured interferometrically using a reference flat with RMS surface figure  $\lambda/100$  kept after the CLA. The procedure similar to the alignment of M1 mirror was repeated. The RMS error inferred from the interferogram was 16.8nm.

#### 4.1.4. Alignment of Quaternary Mirror (M4) and Spectrograph Imaging Lens

After aligning the collimating lens assembly (CLA), other components such as M4, Dichroic Beam Splitter-1 (DBS-1) and spectrograph imaging lens were mounted on the optical bench at their respective nominal positions. Reference flat with RMS surface figure  $\lambda/100$  was mounted at the focal plane of the spectrograph imaging lens. Tilt of the reference flat was adjusted such that the focused beam traverses back in the same path to the interferometer to measure the wavefront error. Following the procedure of M1 mirror alignment, the wavefront error was found to be 13.7nm at the spectrograph multi-slit plane. The procedure was repeated after mounting the fold mirrors FM1, FM2 and FM3.

#### 4.1.5. Alignment of Continuum channel

Alignment of the continuum imaging lens and 5000Å detector was done by measuring the Point Spread Function (PSF) at the focal plane of the continuum channel. In the continuum channel 80% of the energy was contained in  $17.5\mu\text{m}$  size (the design value was  $16\mu\text{m}$ ). After completion of the interferometric alignment of all the optical sub-assemblies, secondary mirror was replaced with the actual flight mirror M2 with the hole. Then, detectors were mounted and ground calibration of the instrument was performed, in both air and vacuum (Prasad et al. 2023).

#### 4.1.6. Alignment of Spectroscopic Channels

Main optical assemblies of the spectroscopic channels in the VELC are Littrow Lens Assembly (LLA) and diffraction grating. To align the LLA interferometrically, a flat mirror with RMS surface figure  $\lambda/40$  was used in place of the grating. Field lens and LLA were mounted at their nominal positions. Orientation of the flat mirror was adjusted to generate the required angle of incidence. De-center and tilts of the field lens and LLA were adjusted to minimize the wavefront error at the focal plane of LLA. The interferometric maps showed RMS wavefront errors of 54.6nm and 54.7nm for the 5303Å and the 7892Å channels, respectively.

## 5. Laboratory Calibration of the instrument

Generally, the different observing channels in the payload must be calibrated in the laboratory using a light beam whose characteristics are similar to that in the regular observations in space. In case of VELC, the instrument has a FoV up to  $3R_{\odot}$  to study the solar corona with a cone angle of  $1.6^{\circ}$ . The solar beam (i.e. sun disk) has a cone angle of  $0.53^{\circ}$ . Feasibility of transmitting the sunlight inside the laboratory by using a coelostat on the rooftop and fold mirror was explored. But, this was not possible in view of the nature of the laboratory building and considering the extreme clean conditions (class 10) of the environment required for the payload to minimize the scatter in the instrument. Further, in spite of the laboratory measurements, instrument parameters need to be calibrated

onboard as these may change due to various factors while integrating with the spacecraft on ground, and in space. We measured some of the parameters of the instruments in the laboratory at various stages of testing such as thermal cycle, vibrations and other environment tests, both before and after integrating the payload with the spacecraft. We found that the parameters such as dark current, fixed pattern noise, response to light signal, stability of the images on the detectors, etc. remained similar and stable during all the stages of integration of the payload with the spacecraft.

### 5.1. Wavelength calibration using sunlight

We were able to transmit the sunlight inside the laboratory using a 2mm fiber bundle. The light beam was expanded using a lens system, and directed at the slits of the spectrograph. The purpose of this experiment was to align the spectrograph and detectors to record the required part of the spectra. Figure 3 shows the spectra of Sun for the four slits, and the spectral profile around the 5303Å wavelength region in the left and right panels, respectively. The estimated dispersion from the separation between the two strong solar disk absorption lines at 5300.7Å & 5302.3Å is  $\approx 0.0284\text{Å}$  per pixel. This is in good agreement with the design value 0.028Å (Table 1 and Section 3.6). The FWHM of the lines are  $\approx 0.25\text{Å}$ . This is consistent with the expected value after taking into consideration the natural and instrumental broadening. The left and right panels of Figure 4 shows the spectra and its profile for 7892Å wavelength region. The absorption lines have been marked in the spectral profiles. All the absorption lines in the 7892Å spectra are due to water vapor in the Earth's atmosphere. The estimated dispersion from the separation between the two strong absorption lines at 7891.9Å & 7893.5Å is  $\approx 0.0313\text{Å}$  per pixel. This is in good agreement with the design value 0.031Å (Table 1 and Section 3.6). The FWHM of the lines in this case is  $\approx 0.30\text{Å}$ . These observations confirm the alignment of detectors at the required wavelength region. The shape of the spectral profiles in the in-orbit observations are likely to be different due to different cone angle of the light beam, but the wavelength region will remain the same. In the laboratory test, the light is a diverging solar beam due to the use of an expander lens assembly. The coronal light in-orbit will be a converging beam with cone angle of  $1.6^\circ$  passing through the narrow band filters. The spectra around 10747Å could not be recorded due to cloudy sky conditions. The alignment of IR detectors was done using a tungsten lamp and narrow band filter. This procedure helps in seeing the spectrum due to each slit without absorption lines. The transmission curve of the filter was compared with that measured by the vendor to confirm the alignment.

## 6. On-orbit testing and calibration

The spacecraft was launched on September 2, 2023 and injected in the 'halo' orbit around the Sun-Earth Lagrangian L1 position on January 6, 2024. Some of the basic operations performed on the instrument have confirmed that all the



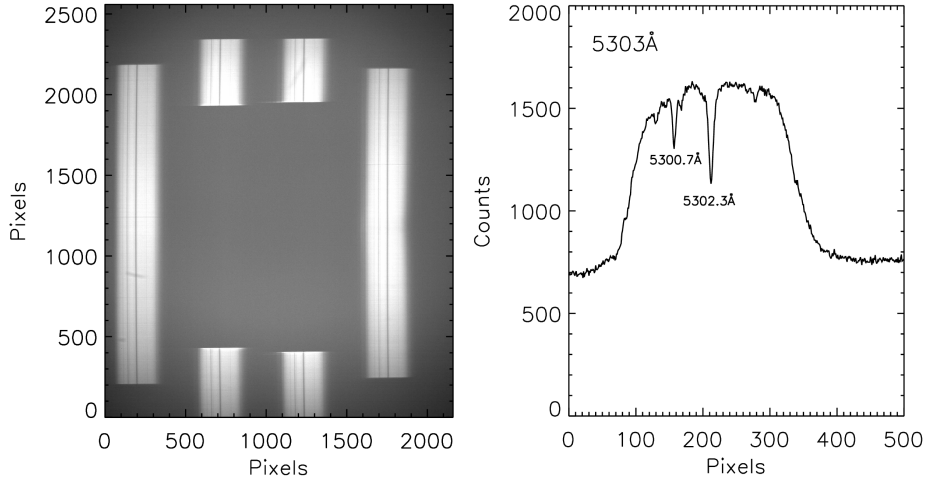


**Figure 3.** The left panel shows the spectra around  $5303\text{\AA}$  obtained with the sunlight transmitted inside the laboratory using a fibre bundle. The slits are 1, 2, 3 & 4 from the left to right. Unlike slits 1 & 4, the middle region of slits 2 & 3 are not noticeable because of the occulter. The right panel shows the spectral profile near the center of slit-1.

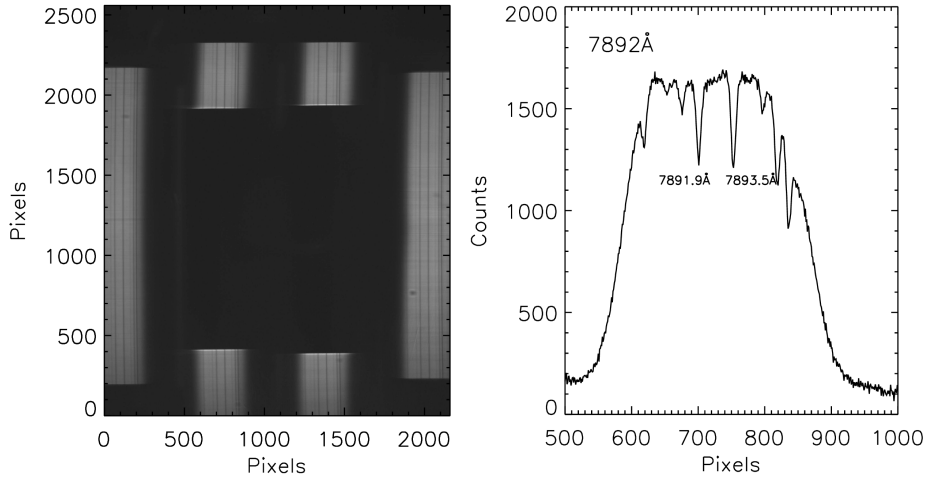


**Figure 4.** Same as Figure 3 but for  $7892\text{\AA}$ . The right panel shows the spectral profile near the center of slit-2 below the occulter.

components are in good aligned condition. The detectors, control units and data acquisition systems are working well. There is some offset between the optic axis of the VELC and that of the spacecraft. Due to this, when spacecraft is pointed towards the centre of the Sun, the image of solar disk light does not fall exactly at the hole in the M2 mirror (occulter). Hence, part of the solar disk image is formed on the detector. The use of ND filter and its smaller aperture (45mm) helps in imaging the part of solar disk as seen in Figure 5 in the continuum channel. The exposure time was 5msec.

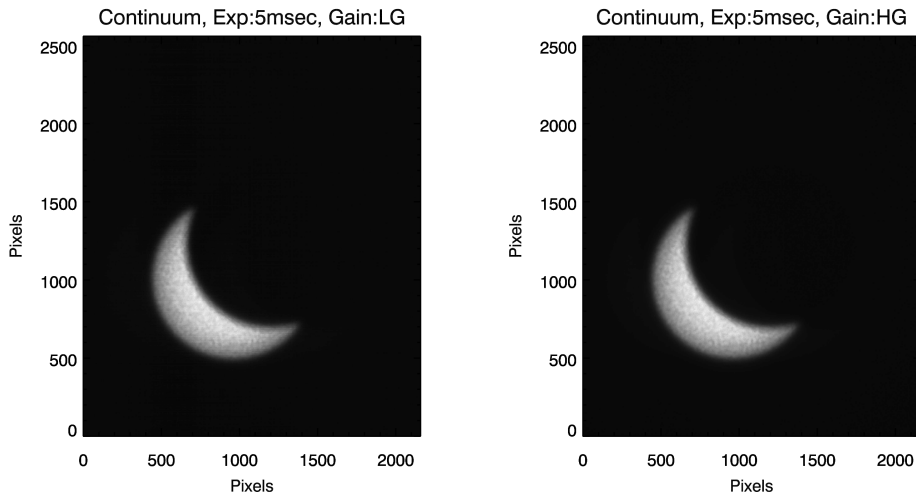


**Figure 5.** The left and right panels show the continuum channel images of a portion of the Sun's disk in low and high gain when the spacecraft was pointed towards the centre of the Sun. The images show the offset between spacecraft and VELC reference axes.

### 6.1. Pointing of satellite

After injection of the satellite into the ‘halo’ orbit as mentioned in the previous paragraph, it was pointed towards Sun using the computed coordinates. The images in continuum showed that Sun center was off from the VELC occulter center by  $\approx 7'$ , in both the roll and pitch directions (Figure 5). Then satellite pointing coordinates were changed using the above computed values, and images in continuum channel were obtained. The observations indicated that the Sun center was still off, but by a smaller margin. To align the center of the Sun with that of occulter (hole in M2 mirror) accurately, the satellite pointing was changed by  $\approx 1'$ , in steps of  $10''$  in both the roll and pitch directions. The coordinates where there was symmetric illumination around the occulter were considered. In this position, the Sun and occulter centers coincides within an uncertainty of  $10''$ . Trial observations on several days showed that the corrections to the satellite pointing coordinates to align both the center of the Sun and occulter centers are same and stable. If any misalignment between the two centers is indicated by the observations, similar exercise will be carried out to point the satellite in the required direction.

### 6.2. ‘Dark’ signal measurements

To carry out ‘dark’ signal measurements on ground, we had installed the detector head in a thermally control vacuum tank in laboratory. The glass windows were closed with thick layers of black paper and cloth. Measurements were obtained with different exposure times (Muthu Priyal et al. 2023) at the temperature of  $22^\circ\text{C}$ , the expected ambient temperature of the payload during the regular observations in-orbit. ‘Dark’ signal measurements in-orbit were obtained by off-pointing the satellite to  $15^\circ$  from the Sun center, so that no sunlight enters the

payload. The shutter in front of the VELC EA was kept closed (Section 3.1). Both the ground and in-orbit measurements agree well.

### 6.3. Variation of signal with exposure time for continuum channel

We find that the values of in-orbit ‘dark’ counts for the detectors in VELC are similar to those at the ground level. But the variation (fixed pattern noise) in the ‘dark’ count appears to be different than that observed at the laboratory. This may be due to change in the electronics for data acquisition, and the harness cables used. The left and right panels in Figure 6 shows the variation of detector count with exposure time for 1X gain onboard (using the solar image seen in Figure 5) and in the laboratory with uniform light source, respectively. The exposure times are different in the two cases because of the nature of the light sources. The detector response w.r.t to the exposure times are linear in both the cases.

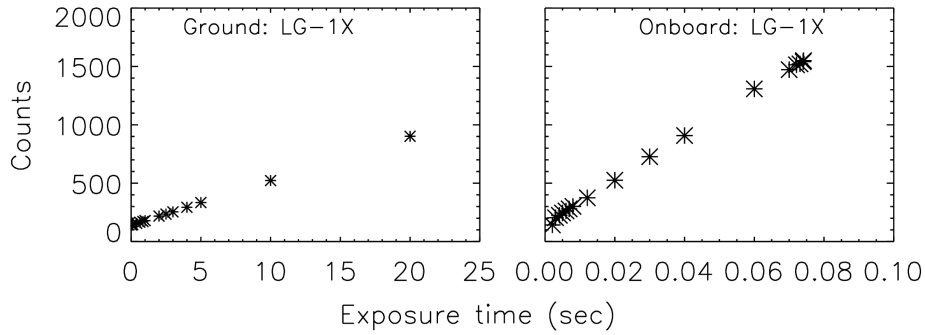


**Figure 6.** Left and right panels show variation in the continuum channel detector mean count (light-dark) for 1X gain as a function of exposure time for ground and in-orbit, respectively. Exposure times in the two cases are different because the characteristics of the respective light beams are different.

### 6.4. Identification of hot/dead pixels

In the case of CMOS detectors, neither the ‘dark’ frames nor the images obtained with uniform light illumination showed any hot/dead pixels. None of the pixels indicated extreme or very low signal with exposure times in the range 0.1 - 100sec. But in the case of IR detector, a particular location always indicated extreme signal irrespective of the exposure time. The corresponding area expanded to the neighbouring pixels for larger exposure times (Muthu Priyal et al. 2023).

### 6.5. Data quality index

The observed data are compressed in the binary format on-board the satellite, transmitted to the ground station, decompressed, and then disseminated to the computer center at Indian Institute of Astrophysics. We find that sometimes data in some rows of the image are not received in this process. Zeros are included for the missing rows/data. Depending on the number of missing rows, the images are labeled as either good or average or poor, and indicated in the header for the corresponding data files.

## 6.6. Spectroscopic observation

While obtaining images of the part of the solar disk through ND filter, spectroscopic observations in all the three channels (5303Å, 7892Å, and 10747Å) were also carried out. Left panel of Figure 7 shows the spectra due to slit 1 & lower portion of slit-2. The sunlight was incident partially on these slits (Figure 5). Middle and right panel of Figure 7 show profiles of the spectra obtained in-orbit and in the laboratory, respectively. The wavelengths of the identified absorption lines have been marked in each case. The transmission profiles of the filter appear different as the cone angle and angle of the beam with respect to filter are different in the two cases. The transmission curve of the filter is expected to change further for the coronal observations as the cone angle of the beam passing through the narrow band filter will increase. The 5303Å emission line will be adjacent to the absorption line at 5302.3Å. The width of emission line will be large, almost ten times that of the absorption line because of the high temperature of coronal plasma leading to thermal broadening of emission lines. We chose a region of interest (ROI) in the continuum portion of the disk spectrum avoiding the absorption line. Same ROI was selected for the data with different exposure times. Left panel of Figure 8 shows the signal as a function of exposure time for the low gain (1X) observations. For comparison we have plotted the signal Vs exposure time in the right panel for the same detector using data obtained in the laboratory with uniform light source. The detector response w.r.t to the exposure times are linear in both the cases.

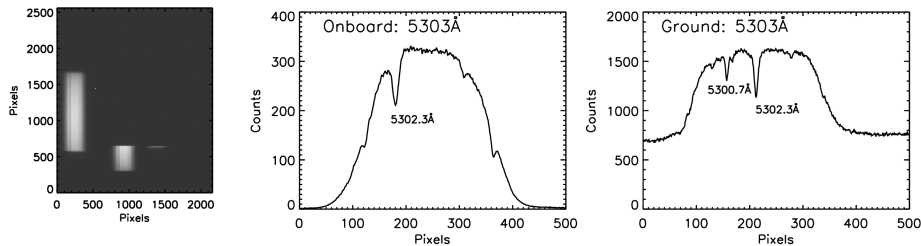


**Figure 7.** Left panel shows the in-orbit spectrum of the solar disk around 5303Å obtained through the ND filter in the EA shutter closed condition (Section 3.1). The sunlight was incident partially on slits 1 & 2 of the spectrograph (Figure 5). The middle and right panels show typical profiles of the spectra of sunlight for the in-orbit and ground observations, respectively.

Similar analysis was carried out for the spectra obtained around the 7892Å line. Figure 9 shows the spectra and profiles of the 7892Å wavelength region obtained in-orbit and the laboratory. The strong absorption lines observed during the tests in laboratory are due to water vapour in the atmosphere. Hence, these absorption lines are not seen in the in-orbit spectrum. Left and right panels of the Figure 10 show the counts for the continuum portion of the spectrum as a function of exposure time for the laboratory and in-orbit observations at 1X gain. Observations at other gains of the cameras show expected performance. The in-orbit spectrum around 10747Å was noisy and difficult to analyze.

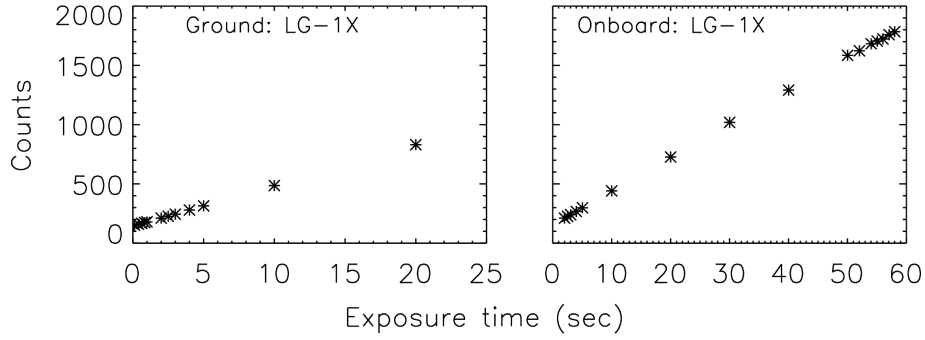


**Figure 8.** Left and right panels show the count at the continuum portion of the spectrum around  $5303\text{\AA}$  as a function of exposure time for laboratory and in-orbit observations, respectively. The X-axis and Y-axis scales are different due to difference in the nature of the light sources.

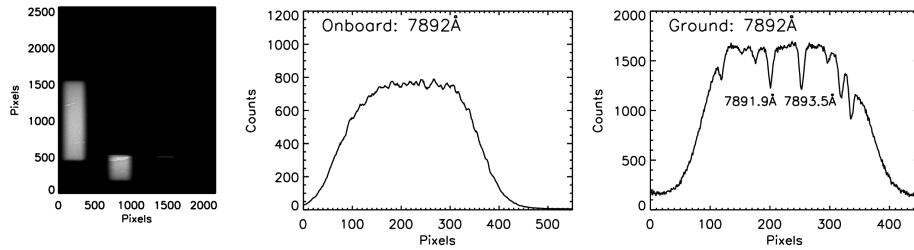


**Figure 9.** Left panel of the figure shows the in-orbit spectrum of the solar disk around  $7892\text{\AA}$  wavelength regions obtained through the ND filter in the EA shutter closed condition (Section 3.1). The sunlight was incident only on slits 1 & 2 of the spectrograph (Figure 5). The middle and the right panels show typical profiles of the spectra of sunlight for the in-orbit and ground observations, respectively.

### 6.6.1. Raster scan observations

We carried out raster scan observations to confirm the working of LSM. The spectra in  $5303\text{\AA}$ ,  $7892\text{\AA}$  and  $10747\text{\AA}$  (IR) channels were obtained with exposure times of 4sec, 2sec, 20sec respectively, with 1X and 10X gains simultaneously. LSM was moved from  $-940\mu\text{m}$  to  $+940\mu\text{m}$  in steps of  $20\mu\text{m}$  (Section 3.5). Generally parameters such as central wavelength of the line, its intensity and width need to be computed to study the spatial and temporal variations. The solar corona cannot be observed in the EA shutter closed condition (Section 3.1). So, we decided to generate intensity image of the part of solar disk (Figure 5) from the spectroscopic observations and compare with the corresponding image obtained in the continuum channel. For this purpose, we considered the average intensity of six pixels in the wavelength/dispersion direction, at the specified wavelength in the continuum. This was uniformly followed for all the locations along the length of slit (spatial direction) and for all the images of the raster scan. Six pixels average was considered for  $5303\text{\AA}$  and  $7892\text{\AA}$  channels since their size ( $6 \times 6.5\mu\text{m}$ ) is close to the LSM step size of  $20\mu\text{m}$  and the equivalent  $40\mu\text{m}$  shift of the image at the slit plane (Section 2.5). Figure 11(a) shows part of the solar image taken in continuum channel, and Figure 11(b) shows the image

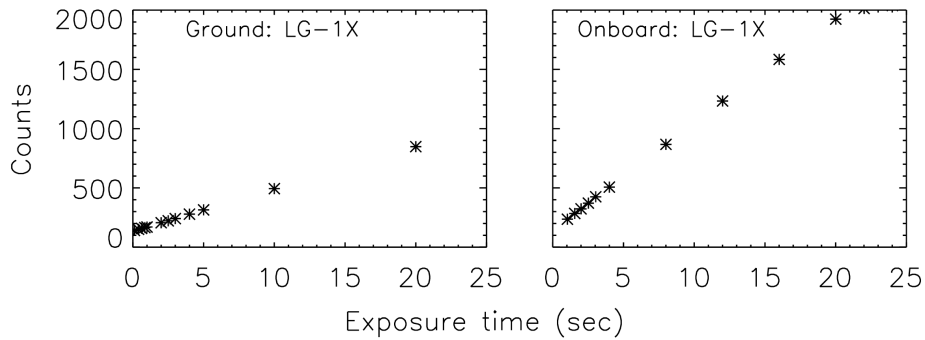


**Figure 10.** Left and right panels of the figure show the count at the continuum portion of the spectrum around  $7892\text{\AA}$  as a function of exposure time for ground and in-orbit observations, respectively. The X-axis and Y-axis scales are different due to difference in light source.

constructed from the raster scan observations. The raster scan image confirms the smooth functioning of LSM. Note that the continuum and raster scan images have different spatial scales, thus appear different in size.

### 6.7. Conversion of count measurements to standard units

Solar disk measurements at the continuum portion of the spectrum can be used as a standard source as it varies by  $\approx 0.2\%$  only over a solar cycle. Therefore, we obtained the disk spectra via the 45mm aperture neutral density filter (ND) when the EA shutter was closed (Section 3.1) and satellite was off-pointed by  $16'$  from the Sun center. The ND filter has a transmission of  $0.64 \times 10^{-4}$  at  $5303\text{\AA}$ . We find that average count per pixel is  $\approx 30$  in the continuum portion of the spectrum adjacent to  $5303\text{\AA}$  emission line. The above count is equivalent to  $\approx 176 \times 10^6$  when the 147mm EA is open and the ND filter is not present in the light path. The solar flux at the center of disk image is  $3.0458 \times 10^6$  ergs/sec/cm<sup>2</sup>/Å/st at  $5303\text{\AA}$ . Hence, one count is equal to  $0.0173$  ergs/sec/cm<sup>2</sup>/Å/sr. The conversion factor will be verified once every three months by carrying out similar observations. The observed peak intensity of the emission line in the corona varies between 15 and 100 at  $1.1R_{\odot}$  for the bright regions. Considering the average peak intensity of 57.5 counts for the emission line in the observed coronal region and a typical line-width of  $0.9\text{\AA}$ , the total intensity of the emission line is  $= 57.5 \times (0.9/0.0284) \times 0.0173 = 32$  ergs/sec/cm<sup>2</sup>/Å/sr. This agrees well with 40 ergs/sec/cm<sup>2</sup>/Å/sr reported by Koutchmy, and Nitschelm (1983); Singh et al. (2019).

## 7. Coronal observations

Considering the offset between the satellite and VELC axis, the satellite was off-pointed such that the VELC optical axis points towards the center of the Sun and the image of latter lies at the center of the hole in the M2 mirror (occultor). Then, we carried out observations in continuum channel to image

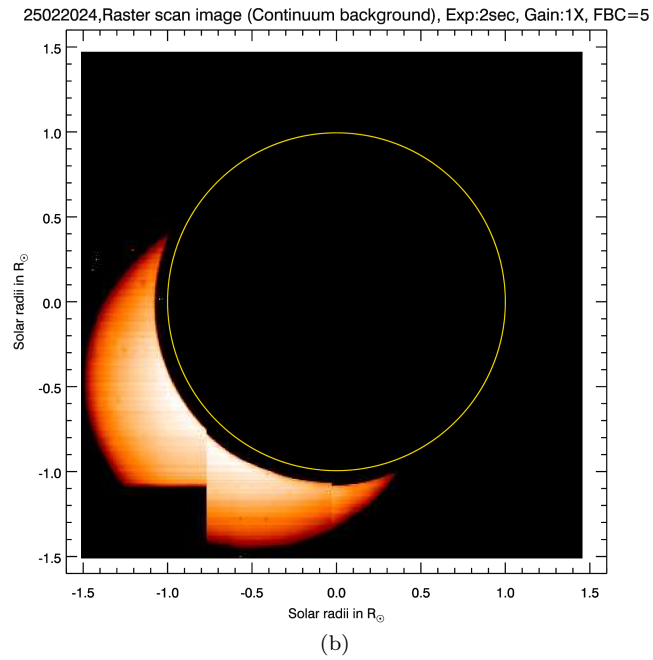
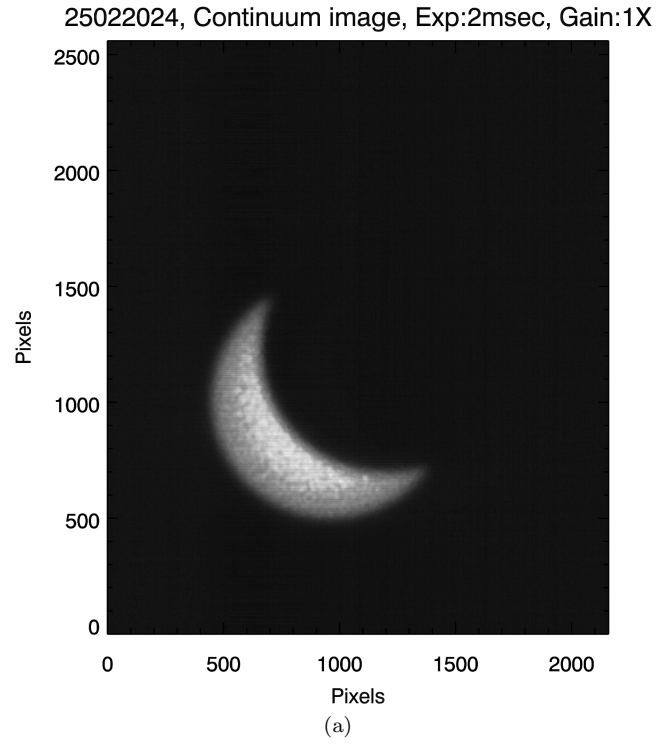


**Figure 11.** Figure (a) and (b) show the continuum image, and the raster scan image constructed from  $5303\text{\AA}$  observations, respectively. The black circular area in both the images is the VELC occulter. The yellow open circle in the raster scan image indicates the Sun disk size. The missing portion in the lower left corner of raster scan image is due to the FoV of slit-1.

the solar corona, and spectroscopic channels around three emission lines. The data in continuum, 7892Å and 10747Å channels are noisy. Hence we report observations in the 5303Å channel alone.

### 7.1. Sit and stare observations

It is possible to locate the image of the corona at the desired position with respect to the slit(s) by moving the LSM. By carrying out observations at various position of LSM from +940 $\mu$ m to -940 $\mu$ m, we found that the east edge of the occulter is at slit 1 when the LSM is at +160 $\mu$ m position. Likewise, for -60 $\mu$ m position of the LSM the west edge of the occulter is at slit 4 (refer Figure 3 for the slit numbers). At LSM position of +110 $\mu$ m, the positions of the slits are symmetric with respect to Sun in the east-west direction. Slits 1 & 4 lie on the east and west side of the solar image. We have carried out observations at different cadences in the range 5-90sec. The high cadence observations are made for short duration to study periodic oscillations in the spectra of coronal structures, thereby the existence of waves, if present. The low cadence (60–90sec) observations will be used to study the dynamics of CMEs.

#### 7.1.1. Flat-fielding the spectrum

We have limitations in obtaining flat-field data for the continuum and spectroscopic channels. Since clean room conditions of class 10 are to be maintained to minimize scattering inside the instrument during the laboratory tests, it was very difficult to create light beam of size and f-ratio similar to that of the expected coronal beam in the regular in-orbit observations. So, we obtained flat-field images in all the four channels with a uniform source created using Labsphere. Thus, these images record the fixed pattern noise of the detector only, and not intensity vignetting due to optics. We found that the in-orbit fixed pattern noise differs from that obtained in the laboratory (Section 4.1).

Generally, it is advisable to keep the narrow band filter close to entrance slit of the spectrograph. In this position, small portion of the filter in width (dispersion direction) will be used. But, due to observational requirements in different wavelengths, we have kept the narrow band filters close to the detectors in each channel. This way, a large width of the filter about 3mm (transmission width of the filter) is used to record the spectrum. Different portions of the filter have different transmission,  $\approx$ 1-2%. Also, the transmission profile of the filter varies with the angle of incident beam. These can also cause some pattern in the recorded spectrum. Therefore, the use of average transmission profile creates large amount of uncertainty in the spectrum. We have attempted to correct each spectrum for the transmission curve of the filter after performing the flat-field correction. It works well for the nearly flat portion of the transmission curve of the filter at the middle, but leaves significant differences for edge portions of the transmission curve. Therefore, we have considered only the central portion of the spectrum as seen in the middle panel of Figure 14 to derive the various parameters of emission line.

The use of flat-field images obtained in the laboratory for the in-orbit data improves the quality of image but not sufficient to accurately study the emission



profiles. We found that fixed pattern noise for the in-orbit observations differs from that obtained in the laboratory. The in-orbit images in Figures 5 & 11 show granular structures whereas the images in Figures 3 & 4 obtained on ground do not show such granular structure. We have attempted to remove the fixed pattern noise in the in-orbit observations by using the spectral images obtained for LSM position at  $+940\mu\text{m}$  and  $-940\mu\text{m}$  where the emission at  $5303\text{\AA}$  is negligible. Then, we constructed a flat-field image by interpolating the data for locations at the absorption lines, one for the data obtained for LSM positions between  $0\mu\text{m}$  and  $+940\mu\text{m}$  and other for  $0\mu\text{m}$  and  $-940\mu\text{m}$ . The use of this flat-field image improves the quality of spectral image significantly. It works well with the data obtained at different days, even though this is not the standard procedure to perform the flat-field correction.

#### *7.1.2. Stability of the spectra in dispersion direction*

Generally, spectra obtained with ground based observations do not shift on the detector in the dispersion and spatial directions due to the stability of the spectrograph. Our time sequence observations at fixed locations of the image show that spectral images are not stable in the dispersion (wavelength) direction. We found that the minimum in the absorption line at  $5302.3\text{\AA}$  oscillates around the mean position by about 5 pixels ( $\sim 140\text{m}\text{\AA}$ ). This may be due to oscillations in some optical component or the detector. It is not clear why and how it happens. We observed on number of days and concluded that the shift in the spectrum on the detector is not due to Doppler velocity of the plasma, but due to the instrument. Therefore, we have aligned all the spectra to the mean position of the absorption line adjacent to the  $5303\text{\AA}$  emission line in the first slit (pixel no. 181). After alignment, the variations in the center of the absorption line is within  $\pm 1$  pixel.

#### *7.1.3. Curvature correction for the spectra*

Generally, the observed spectrum can be curved because of spherical aberrations in various optical components, especially in the short focal length spectrograph. The VELC spectra obtained showed curvature in the absorption line at  $5302.3\text{\AA}$  even though the entrance slit is straight. The difference in the location of absorption line is  $\approx 8$  pixels between the edges and centre of the slit. We determined the center of the absorption line at each spatial location along the slit. A polynomial fit was computed for the data corresponding to the center of the absorption line. Then, spectrum at each spatial location was shifted by the difference observed between the reference position of the absorption line and the polynomial fit value. After this, the error in the center of the absorption line was found to be  $\pm 1$  pixel ( $28.4\text{m}\text{\AA}$  for the  $5302.3\text{\AA}$  line) at random, indicating a good alignment.

#### *7.1.4. Effect of satellite drift*

We also found that the coronal spectra show oscillatory pattern along the slit (spatial direction). We obtained spectra with an exposure time of 5sec and

cadence of 50sec by keeping the LSM at  $-60\mu\text{m}$  for about 9h on August 22, 2024. Figure 12 shows the intensity at various locations (i.e. position angles, measured counter clockwise from the solar north through east) along slit-4 with time. It is a long duration data set obtained at low cadence. The oscillatory pattern as a function of time is clearly evident. This may be due to satellite pointing or some unknown reason. The shift is  $\approx\pm 15''$  about the mean position. We attempted to compensate for this drift along the slit using the brightest feature seen in Figure 12 near position angle  $\approx 260^\circ$ . We selected consecutive 20-40 intensity locations along the spatial direction around the bright feature, and determined the location of the maximum intensity in each spectrum of the time sequence observations. Then we computed the mean spatial location of the maximum intensity. Assuming the location of the maximum intensity does not vary much with time, we align all the spatial locations at each time sequence in the observations to the above mentioned mean position. The above work is in progress and will be reported separately. Note that in the absence of a bright feature, there can be uncertainties in determining the location of the maximum intensity.

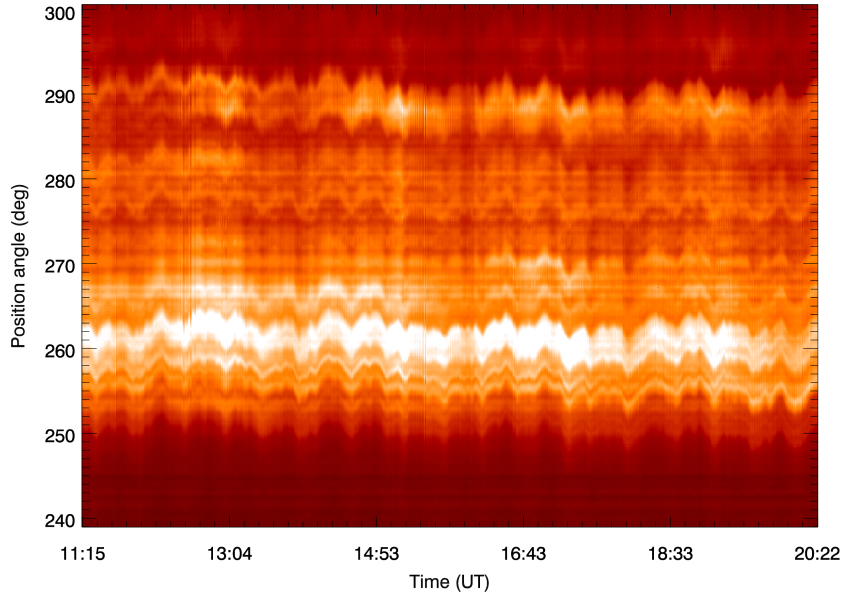


**Figure 12.** Sit and stare observations of coronal intensity at  $5303\text{\AA}$ . X-axis and Y-axis represents time and position angle, respectively. Variations in the intensity between different position angles are due to the brightness of the coronal structures at different locations. The oscillatory pattern along the X-axis may be due to the drift of the satellite or some unknown factor.

### 7.1.5. Estimate of scatter light

It is difficult to estimate the scatter in the instrument as coronal and scattered light are always present in the continuum and spectral images. An indirect approach may help to get an estimate of the scattered light in the spectrograph. We assume that contribution of the continuum coronal light is about 2% of the emission light in the  $5303\text{\AA}$  line (equivalent width of emission line = 60), and can be neglected. Therefore, continuum signal in the coronal spectra is mostly because of scattered light in the instrument. We found in Section 6.7 that solar disk count is  $176 \times 10^6/\text{pixel}/\text{sec}$  for 1X gain of the detector in the EA shutter open observations (147mm EA, without the ND filter). The average count at the continuum portion of the coronal spectrum is  $\approx 200/\text{pixel}/\text{sec}$  for 1X gain, for the slit position at  $1.13R_{\odot}$ . It may be noted that there are variations in the above count for different days of observations. The ratio of continuum signal to the disk light in the coronal spectra is  $\approx 1.1 \times 10^{-6}$ . The ratio is expected to be much higher close to the solar limb since scattered light decreases exponentially. Note that the emission corona signal at  $1.13R_{\odot}$  is  $\sim 10^{-8}$ . It varies depending on the coronal structures (Section 6.7).

### 7.1.6. Data analysis

We have analysed the data obtained at number of LSM positions with different gains and exposure times. We find that spectral images with 5sec exposure in low gain mode (1X) are of comparatively good quality as compared to other exposure times. Exposure times  $>5\text{sec}$  leads to saturation of the spectra near the solar limb. Adding the spectra onboard to increase the SNR has a drawback. The spectra obtained by adding the frames onboard get averaged in the dispersion and spatial directions as spectrum oscillates in both these directions. Left side panel of Figure 13 shows a typical spectrum obtained with 5sec exposure at LSM at  $+160\mu\text{m}$  in sit and stare mode of observations. The middle panel shows the spectrum after curvature correction, dark subtraction and flat-field correction. The right side panel shows the spectrum after sky subtraction (scattered light removal).

We notice that the amplitude of signal due to emission line at  $5303\text{\AA}$  is about 10%–15% whereas background count is 85%–90% in these observations. This is the case in most of the observations. For observations made by Singh, Sakurai, and Ichimoto (2003a) with 25cm coronagraph at Norikura observatory, the emission line signal and the background are about 60% and 40%, respectively. It is not clear why the corresponding values are significantly different in VELC observations. Probably, some stray light is entering the instrument. This assumption gains support from the observations of the deep sky in continuum channel. The satellite was off pointed by about  $75^\circ$ , looking far away from the Sun and images of Sirius A (stellar observation) were obtained in the continuum channel. The detector showed high background count, indicating the existence of stray light.

Left panel of Figure 14 indicates the observed profile around  $5303\text{\AA}$  at a spatial location for the spectra shown in the left panel of Figure 13. Middle

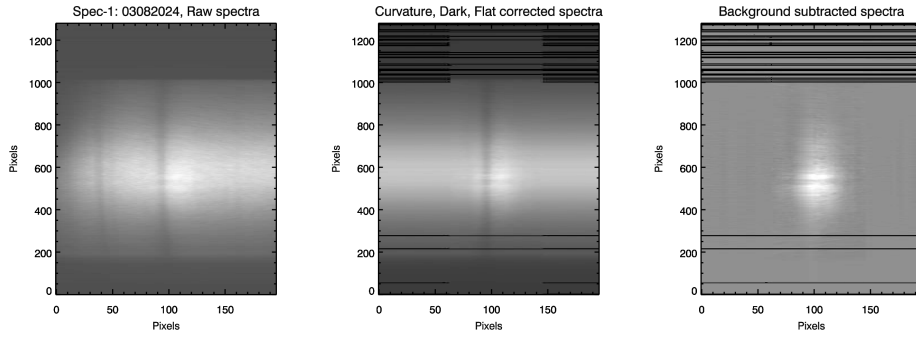


**Figure 13.** Left panel shows the spectrum around  $5303\text{\AA}$  for 1X gain obtained with 5sec exposure time on August 3, 2024. X- and Y- axes represent dispersion and spatial directions, respectively. Middle panel shows the spectrum after curvature, dark and flat-field corrections. Right side panel shows the spectrum after sky subtraction (scattered light).

and right panels of Figure 14 show the profiles for the spectra shown in middle and right panels of Figure 13, respectively. The red colour profile in the right side panel is the Gaussian fit for the corrected profile. The parameters such as intensity, FWHM, and Doppler velocity of the line profile have been computed from the Gaussian fit, and stored as a function of spatial location and time. Figure 15 (a) and (b) show the histograms of FWHM for the data of slit 1 (east) and slit 4 (west) respectively. The values of FWHM for both the slits are in the expected range  $0.5\text{-}1.5\text{\AA}$  considering the temperature ( $1\text{-}3\times 10^6\text{K}$ ) and non-thermal velocity for microscale Fe XIV emission. The values of FWHM have been corrected for the instrumental line width. The difference between the mean values of the FWHM for the solar corona at the east and west edges of the occulter may be due to difference in the physical characteristics of the coronal structures at either location on that day. The larger width of the distribution in the case of slit-1 (east) could be due to contribution from different loops (behind and front) also. We plan to investigate this using larger data set obtained on different days.

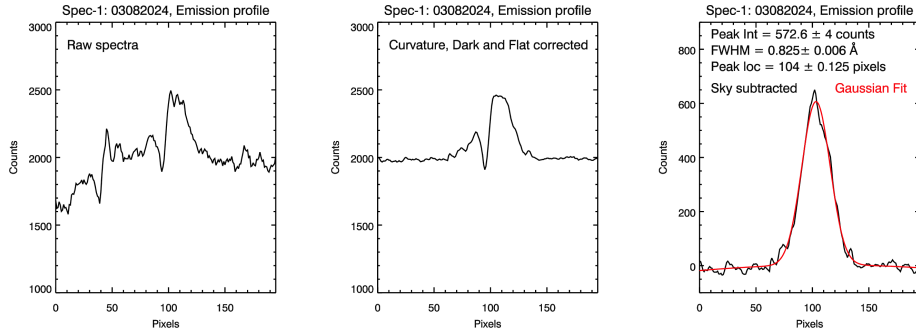


**Figure 14.** Left panel shows the profile around  $5303\text{\AA}$  for 1X gain obtained with 5sec exposure time on August 3, 2024 at a spatial location. Middle panel shows the profile for the spectrum shown in middle panel of Figure 13 after curvature, dark and flat-field corrections. Right side panel shows the profile after sky subtraction (scattered light) along with a Gaussian fit. Parameters along with the SD values of the Gaussian fitted profile are given in panel.

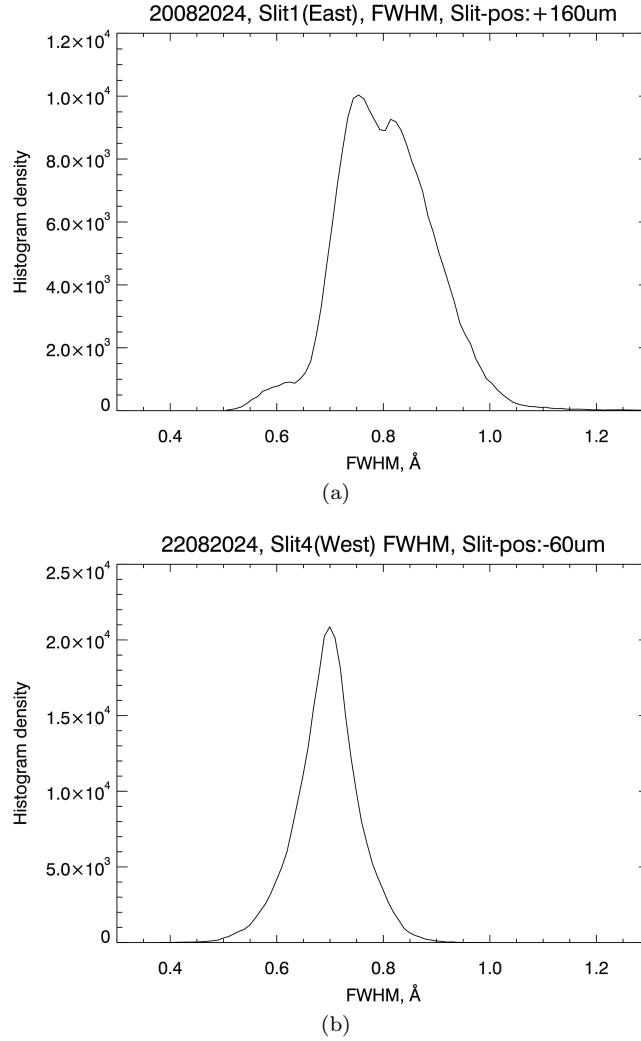


**Figure 15.** Figures (a) & (b) show the histograms of FWHM for the data of slit-1 (east) and slit-4 (west), respectively.

## 7.2. Raster scan observations: Coronal

We carried out raster scan observations with different combination of exposure times, onboard frame binning, different gains of the cameras, and LSM step sizes in all the spectroscopic channels. Considering the spectral images, time required to complete one raster scan, data rate, and data volume per raster scan, we find that the optimum parameters for raster scan observations are: exposure time = 4sec; number of frames binned onboard (i.e. frame binning count, FBC) = 5; camera gains = 1X and 10X; step size =  $20\mu\text{m}$ ; number of steps = 95 ( $-940\mu\text{m}$  to  $+940\mu\text{m}$ ); time for one raster scan = 32min. Note that raster scans can be taken with different parameters to get the data at smaller or larger cadence

depending upon the scientific objective. Data volume should be also considered while planning such observations. Here, we present the results of the raster scan made with the above mentioned parameters. We have analysed the raster scan data using all the steps mentioned earlier for sit and stare mode observations. We computed the parameters such as central wavelength of the emission line, intensity and width of emission line at each spatial location along the slit and for each step of LSM. The peak intensities were determined in counts as shown in the right side panel of Figure 14. The counts can be converted in to solar units considering number of pixels binned and exposure time used during observations as explained in Section 6.7. There are four slits and we analysed the data for each slit separately. After determining the parameters of emission line, we combined the data from all the four slits to form a coronal image. Figure 16 shows a composite of the intensity images of the solar corona observed with VELC in  $5303\text{\AA}$  ( $\text{FoV}\approx 1.5R_{\odot}$ ) and SDO/AIA in  $193\text{\AA}$  ( $\text{FoV}\approx 1.2R_{\odot}$ ). There is a good correspondence between the off-limb structures in the two images. The coronal features above the east and west limbs of the Sun could be noticed in the VELC image. Due to the larger FoV in the VELC, the coronal loops (particularly those above the west limb) could be observed to comparatively larger distances. But no coronal structures could be noticed above the north and south limbs of the Sun. The emission is very weak there. Computing the intensity from emission line profile for weak coronal features is difficult amidst the background continuum. Gaussian fit for the line profile does not converge for weak features and hence we do not notice the latter in both the polar regions. It is to be noted that there are no bright coronal structures near the north and solar limbs in the SDO/AIA image also.

## 8. Summary

We find that background signal in the coronal observations with VELC is large, more than expected. The spectroscopic observations made at  $5303\text{\AA}$  emission line with the 25cm ground based Norikura coronagraph indicate a large ratio ( $\approx 1.5$ ) of emission signal to the background nearby continuum portion of the spectrum as compared to the ratio of  $\approx 0.3$  in the VELC observations. This indicates more scatter light in VELC. Larger than design microroughness of the M1 mirror is likely to increase the scattering, but not certain if that is the only cause. The observations in the  $5303\text{\AA}$  line are useful in the sit and stare mode as well as raster scan mode (Ramesh et al. 2024). The authors reported direct proof of coronal dimming during the occurrence of a CME. The sit and stare mode with high cadence observations will help to study oscillations in the coronal structures, thereby existence of waves, flows and dynamics of corona. The sit and stare mode observations with low cadence for long duration will help to study the CMEs and other energetic events along with observations in the radio wavelengths (Ramesh et al. 1998, 2012; Kathiravan, Ramesh, and Subramanian 2002; Hariharan et al. 2014). The raster scan observations will help to study the variation in emission line parameters spatially, thereby the physical characteristics of coronal structures. Raster scan observations will also permit

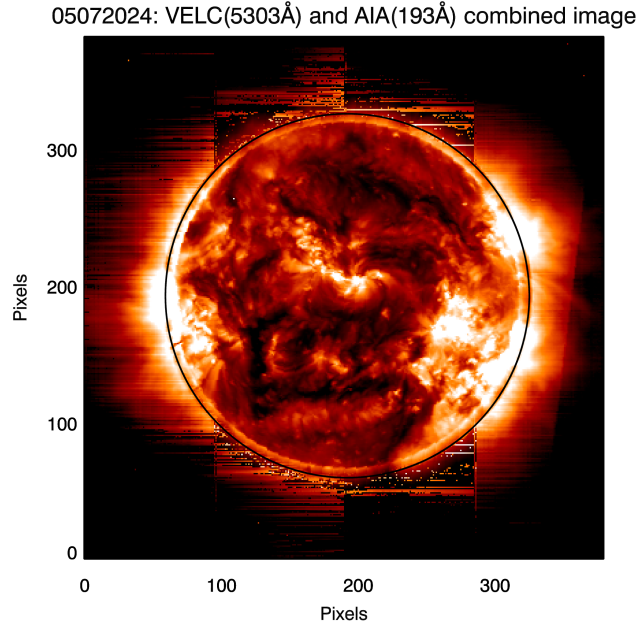


**Figure 16.** Composite intensity image of the solar corona in 5303Å (VELC) and 193Å (SDO/AIA) on July 5, 2024. The black circle represents the VELC occulter.

to investigate the long term variations in the solar corona. Joint observations with VELC and instruments like AIA, uCoMP, PROBA-3 are expected to be a valuable tool to understand the near-Sun corona.

The spectroscopic observations carried out in the 7892Å channel with different exposure times, and adding number of spectra to enhance the signal to noise ratio has not resulted in detection of emission component at 7892Å wavelength. We tried to do this in all the gains of the camera but the emission line signal was elusive. Also, emission signal at 7892Å line is less as compared to 5303Å. The use of narrow band filter introduces noise in the data as explained in Section 7.1.1. The ground based observations indicated that data with IR detector has large noise, both in low and high gain mode of operation. The noise in the in-orbit data has increased further, probably due to EMI. Repeated experiments for 10747Å channel, similar to 7892Å channel, has not yielded positive results. At present, it appears that the use of data from these channels for scientific purposes might be difficult. Attempts may be made in the future to retrieve useful data from these two channels. Some of the scientific objectives, for example temperature determination from the intensity ratios of two emission lines, magnetic field measurements, etc. will not be possible till then. In spite of these limitations, continuous observation in the 5303Å channel will be very valuable to study the corona, especially energetic events.

## Acknowledgments

Aditya-L1 is an observatory class mission which is fully funded and operated by the Indian Space Research Organization (ISRO). We thank all the Scientists and Engineers at the various centres of ISRO and Indian Institute of Astrophysics who have made significant contributions for the VELC payload to reach the present state. The SDO team is acknowledged for online dissemination of their data. We thank the referee for his/her valuable comments which helped us to present the results more clearly.

## Declarations

No funding was received for conducting this study.

## References

- Doyle, J. G., Banerjee, D., Perez, M. E.: 1998, Coronal line-width variations, *Solar Phys.*, **181**, 91–101.
- Hassler, D. M., Rottman, G. J., Orrall, F. Q.: 1990, Absolute Velocities and Center-to-Limb Variations of EUV Emission Lines in the Quiet Sun, *BAAS*, **22**, 815.
- Ichimoto, K., Hara, H., Takeda, A., et al.: 1995, Coordinated Observation of the Solar Corona Using the Norikura Coronagraph and the YOHKOH Soft X-Ray Telescope, *Astrophys. J.*, **445**, 978–981.
- Jelinek, P., Srivastava, A. K., Murawski, K., Kashyap, P., Dwivedi, B. N.: 2015, Spectroscopic Observations and Modelling of Impulsive Alfvén Waves Along a Polar Coronal Jet, *Astron. Astrophys.*, **581**, A131.
- Hariharan, K., Ramesh, R., Kishore, P., Kathiravan, C., Gopalswamy, N.: 2014, An Estimate of the Coronal Magnetic Field near a Solar Coronal Mass Ejection from Low-frequency Radio Observations, *Astrophys. J.*, **795**, 14.
- Kathiravan, C., Ramesh, R., Subramanian, K. R.: 2002, Metric Radio Observations and Ray-tracing Analysis of the Onset Phase of a Solar Eruptive Event, *Astrophys. J.*, **567**, L93–L95.
- Kishore, P., Ramesh, R., Kathiravan, C., Rajalingam, M.: 2015, A Low-Frequency Radio Spectropolarimeter for Observations of the Solar Corona, *Solar Physics*, **290**, 2409–2422.
- Koutchmy, S., Nitschelm, I.: 1983, Photometric analysis of the June 11, 1983 solar corona, *Astron. Astrophys.*, **138**, 161–163.
- Krishna Prasad, S., Jagdev Singh, Ichimoto, K.: 2013, Thermal structure of coronal loops as seen with Norikura coronagraph, *Astrophys. J. Lett.*, **765**, L46.
- Krishna Prasad, S., Jess, D. B., Van Doorselaere, T., Banerjee, D.: 2017, The Damping of Coronal Oscillations, *Astrophys. J.*, **834**, 103.
- Kumar, N., Prasad, B. R., Jagdev Singh., Venkata, S. N.: 2018, Optical design of the visible emission line coronagraph on Indian space solar mission Aditya-L1, *Exp. Astron.*, **45**.
- Kumari, A., Ramesh, R., Kathiravan, C., Wang, T. J., Gopalswamy, N.: 2019, Direct Estimates of the Solar Coronal Magnetic Field Using Contemporaneous Extreme-ultraviolet, Radio, and White-light Observations, *Astrophys. J.*, **881**, 24.
- Muthu Priyal, Jagdev Singh, Prasad, B. R., et al.: 2023, Data processing of visible emission line coronagraph onboard ADITYA-L1, *Adv. Space Res.*, **74**, 547–560.
- Minarovjech, M., Rusin, V., Rybansky, M., Sakurai, T., Ichimoto, K.: 2003, Oscillations in the coronal green-line intensity observed at Lominicky Stit and Norikura Nearly simultaneously, *Solar Phys.*, **213**, 269–290.
- Nagaraaju, K., Prasad, B. R., Bhavana Hegde, S., et al.: 2021, Spectropolarimeter onboard Aditya-L1, polarization modulation and demodulation, *App. Optics*, **60**, 8145–8153.
- Pasachoff, J. M., Babcock, B. A., Russell, K. D., Seaton, D. B.: 2002, Short-Period Waves That Heat the Corona Detected at the 1999 Eclipse, *Solar Phys.*, **207**, 241–257.



- Raju, K. P., Chandrasekhar, T., Ashok, N. M.: 2011, Analysis of coronal green line profiles: Evidence of excess blueshifts, *Astrophys. J.*, **736**, 164.
- Ramesh, R., Subramanian, K. R., Sundara Rajan, M. S., Sastry, Ch. V.: 1998, The Gauribidanur Radioheliograph, *Solar Phys.*, **181**, 439–453.
- Ramesh, R., Subramanian, K. R., Sastry, Ch. V.: 1999, Eclipse Observations of Compact Sources in the Outer Solar Corona, *Solar Phys.*, **185**, 77–85.
- Ramesh, R., Kathiravan, C., Sastry, Ch. V.: 2003, Metric Radio Observations of the Evolution of a “Halo” Coronal Mass Ejection Close to the Sun, *Astrophys. J. Lett.*, **591**, L161–L163.
- Ramesh, R., Nataraj, H. S. Kathiravan, C.: 2006, The Equatorial Background Solar Corona during Solar Minimum, *Astrophys. J.*, **648**, 707–711.
- Ramesh, R., Kathiravan, C., Indrajit V. Barve, Rajalingam, M.: 2012, High Angular Resolution Radio Observations of a Coronal Mass Ejection Source Region at Low Frequencies during a Solar Eclipse, *Astrophys. J.*, **744**, 165.
- Ramesh, R., Muthu Priyal, V., Jagdev Singh., et al.: 2024, New Results on the Onset of a Coronal Mass Ejection from 5303Å Emission Line Observations with VELC/ADITYA-L1, *Astrophys. J. Lett.*, **976**, L6.
- Prasad, B. R., Banerjee, D., Jagdev Singh., et al.: 2017, Visible Emission Line Coronagraph on Aditya-L1, *Curr. Sci.*, **113**, 613–615.
- Prasad, B. R., Venkata, S. N., Natarajan, V., et al.: 2023, Ground calibration of visible emission line coronagraph on board Aditya-L1 mission, *J. Astron. Teles. Inst. Sys.*, **9(4)**, 044001.
- Rusin, V., Minarovjech, M.: 1994, Detection of Small-Scale Dynamics in the Emission Corona, *Solar Coronal Structures. Proc. IAU Coll. 144*, 487–490.
- Samanta, T., Jagdev Singh., Sindhuja, G., Banerjee, D.: 2016, Detection of High-Frequency Oscillations and Damping from Multi-slit Spectroscopic Observations of the Corona, *Solar Phys.*, **291**, 155–174.
- Sasikumar Raja, K., Venkata, S. N., Jagdev Singh., Prasad, B. R.: 2022, Solar coronal magnetic fields and sensitivity requirements for spectropolarimetry channel of VELC onboard Aditya-L1. *Adv. Space Res.*, **69**, 814–822.
- Singh, J., Bappu, M. K. V., Saxena, A. K.: 1982, Eclipse observations of coronal emission lines. I. [Fex] 6374Å profiles at the eclipse of 16 February 1980, *J. Astron. Astrophys.*, **3**, 249–266.
- Singh, J., Cowsik, R., Raveendran, A. V., et al.: 1997, Detection of short-period coronal oscillations during the total solar eclipse of 24 October 1995, *Solar Phys.*, **170**, 235–252.
- Singh, J., Ichimoto, K., Imai, H., Sakurai, T., Takeda, A.: 1999, Spectroscopic Studies of the Solar Corona I. Spatial Variations in Line Parameters of Green and Red Coronal Lines, *Pub. Astron. Soc. Japan*, **51**, 269–276.
- Singh, J., Sakurai, T., Ichimoto, K.: 2003a, Spectroscopic Studies of the Solar Corona. IV. Physical Properties of Coronal Structure *Astrophys. J.*, **585**, 516–523.
- Singh, J., Sakurai, T., Ichimoto, K., Muneer, S.: 2003b, Spectroscopic Studies of the Solar Corona. IV. Physical Properties of Coronal Structure, *Solar Phys.*, **212**, 343–359.
- Singh, J., Sakurai, T., Ichimoto, K., Hagino, M., Yamamoto, T. T.: 2004a, Existence of Nanoparticle Dust Grains in the Inner Solar Corona?, *Astrophys. J.*, **608**, L69–L72.
- Singh, J., Sakurai, T., Ichimoto, K., Watanabe, T.: 2004b, Complex variations in the line-intensity ratio of coronal emission lines with height above the limb, *Astrophys. J. Lett.*, **617**, L81–L84.
- Singh, J., Sakurai, T., Ichimoto, K.: 2006, Do the line widths of coronal emission lines increase with height above the limb?. *Astrophys. J.*, **639**, 475–483.
- Singh, J., Hasan, S. S., Gupta, G. R., Nagaraju, K., Banerjee, D.: 2011a, Spectroscopic Observation of Oscillations in the Corona During the Total Solar Eclipse of 22 July 2009, *Solar Phys.*, **270**, 213–233.
- Singh, J., Prasad, B. R., Venkatakrishnan, P., et al.: 2011b, Proposed visible emission line space solar coronagraph, *Curr. Sci.*, **100**, 167–174.
- Singh, J., Prasad, B. R., Venkata, S., Kumar, A.: 2019, Exploring the outer emission corona spectroscopically by using Visible Emission Line Coronagraph (VELC) on board ADITYA-L1 mission, *Adv. Space Res.*, **64**, 7, 1455–1464.
- Singh, J., Prasad, B. R., Sumana, C., et al.: 2022, Data pipeline architecture and development for VELC onboard Space Solar Mission Aditya-L1, *Adv. Space Res.*, **69**, 2601–2610.
- Tsubaki, T.: 1977, Periodic oscillations found in coronal velocity fields, *Solar Phys.*, **51**, 121–130.
- Venkata, S. N., Prasad, B. R., Singh, J.: 2021, Spectropolarimetry Package for Visible Emission Line Coronagraph (VELC) on board Aditya-L1 Mission. *Exp. Astron.*, **53**, 71–82.

- 
- Venkata, S. N., Prasad, B. R., Nalla, R. K., Singh, J.: 2017, Scatter studies for visible emission line coronagraph on board ADITYA-L1 mission. *JATIS*, **3**, 014002.
- Venkata, S. N., Budhiraju, V. R., Natarajan, V., et al.: 2023a, Performance evaluation of Littrow lens assembly for visible emission line coronagraph (VELC) on board Aditya-L1 mission, *Journal of Optics*, **53** (2), 857–862.
- Venkata, S. N., Bhavana Hegde, S., Utkarsha, D., et al.: 2023b, Calibration of spectropolarimetry package for visible emission line coronagraph (VELC) on board Aditya-L1 mission, *J. Astron. Instr.*, **12**(04), 2350011.
- Venkata, S. N., Sasikumar Raja, K., Prasad, B. R., et al.: 2024, Calibration of spectropolarimetry channel of visible emission line coronagraph onboard Aditya-L1. *Exp. Astron.*, **58**, 6.
- Voulgaris, A. G., Gaintatzis, P. S., Seiradakis, J. H., Pasachoff, J. M., Economou, T. E.: 2012, Spectroscopic Coronal Observations During the Total Solar Eclipse of 11 July 2010, *Solar Phys.*, **278**, 187–200.